Woodchip size effect on combustion temperatures and volatiles in a small-scale fixed bed biomass boiler

Gianluca Caposciutti[a,*], Federica Barontini[b], Chiara Galletti[b], Marco Antonelli[a], Leonardo Tognotti[b], Umberto Desideri[a]

[a]*Department of Energy, Systems, Territory and Constructions Engineering, University of Pisa, Italy*

[b]*Department of Civil and Industrial Engineering, University of Pisa, Italy*

Abstract

Biomass combustion performance is greatly affected by the particle size distribution, which influences heat and mass transport phenomena. The present work investigates the effect of woodchip size distribution on combustion in a 140kW underfeed stoker boiler. Three different fuel sizes were prepared, and their combustion performance was measured by monitoring temperatures inside and above the fire pit and the gas composition above the fuel bed. The gas composition was then correlated to the particle mean diameter. Although minor effects could be detected in the temperature and composition of the flue gases, a more uniform spatial distribution of volatiles was observed when employing bigger woodchips. The present results can improve the understanding of the impact of fuel size on the performance of woodchip-fired boilers and can be valuably used for numerical model validation.

keywords: Biofuels; Fuel size; Biomass combustion; Particles size;

_____

*corresponding author: *Gianluca Caposciutti*; e-mail: *gianluca.caposciutti@ing.unipi.it*

Nomenclature

Abbreviations	
a	air
CL	Centre-Low Point
CM	Centre-Middle Point
CS	Centre-Side Point
CU	Centre-Upper Point
EN	Environnement Bench SA
FC	Fixed Carbon
GC	Gas Chromatograph
ID	Identification Number
LHV	Lower Heating Value
LL	Left-Low Point
LM	Left-Middle Point
LS	Left-Side Point
LU	Left-Upper Point
MMD	Mean Diameter
R	Pearson Coefficient
RL	Right-Low Point
RM	Right-Middle Point
RS	Right-Side Point
RU	Right-Upper Point
SMD	Sauter Mean Diameter
SRF	Short Rotation Forestry
T	Temperature
TC	Thermocouple
VM	Volatile Matter

Y	Mass fraction
Subscripts/Superscripts	
ar	as received
daf	dry ash free basis
db	Dry Basis
e	Exhaust Gas
f	Fuel
in	Inlet
max	Maximum
n	Numeral
p	Primary
s	Secondary
st	Stoichiometric
tot	Total
v	Volume Basis
vol	Volatiles Basis
wt	Weight Basis
Symbols	
d	Diameter
f	Fraction
$\widehat{m}$	Derivative parameter
α	Air To Fuel Ratio
ε	Excess air
λ	Air Split Ratio

21

1. Introduction

In grids dominated by unprogrammable renewable energy sources, biomass can help to provide a smooth transition from fossil fuels to renewable sources [1]. One of the main advantages of biomass-fired systems for micro and distributed generation is the flexibility of use [2,3]. Small scale biomass power plants are much more interesting than larger ones, because of the lower capital costs, logistic expenditures and higher return on investment [4,5]. In Europe, small scale biomass combustion devices burning wood logs, pellets or woodchips of ligneous-cellulosic biomass [6,7], are widely used [8]. Although biomass is a renewable energy source, it is necessary to reduce the pollutant emissions from its combustion. Air staging may significantly reduce pollutant emissions in systems with thermal power between 10 and 50 kW [9–12]. A small amount of oxygen is provided to the primary combustion zone (where drying, pyrolysis and char combustion occur) to limit nitrogen oxides formation and fuel bed temperatures, while the complete oxidation of the combustion products is obtained through a secondary air supply stage above the fuel bed.

The primary combustion zone was investigated in a 50kW biomass boiler by Buchmayr et al. [13], who found that the primary air distribution strongly affects the combustion temperature, and thus volatile release, above the fuel bed. Similar findings were also reported by Caposciutti et al. [14] who observed differences in the spatial distribution of volatiles when using different primary air flow rates in a 140 kW boiler.

However, combustion performance is also dependent on the fuel properties, such as fuel density and size. In particular, the relevance of the latter has been investigated in several pyrolysis and combustion studies.

Bryden et al. [15] developed a wood slab pyrolysis model by using a 1-Dimensional porous domain. They found that a larger particle size produces a thicker char layer on the wood slab, thus significantly influencing the volatiles and tar yields.

Holmgren et al. [16] developed a particle conversion model based on biomass size and shape. They observed that the Initial particle size affected its shrinkage behavior, where larger particles resulted in a slower size variation rate, due to their larger thermal inertia.

Bellais et al. [17] employed a pyrolysis model for large wood particles to assess the effect of the shrinking process in the conversion prediction. A sensitivity analysis showed that the effect of the fuel density was greater than the particle shrinking. However, when initial particle size is reduced, the size variation can strongly influence the pyrolysis reactions and gas propagation.

Lu et al. [18] studied the influence of particle size (between 320 μm and 10 mm) and shape on the heating, drying and reaction rates of biomass in pyrolysis conditions. An entrained flow reactor and a single particle reactor (for larger particles) were used. Moreover, a model was developed to predict the process behavior as a function of the size and shape of the samples. Pyrolysis was found to be mainly influenced by the particle heating rate. This was especially evident for large particles, where volatile yield of all particles decreased with increasing particle size.

More recently, Liu et al. [19] investigated the segregation of solid fuels in a fluidized bed system (i.e., horizontal stirred bed reactor) using discrete element method (DEM) simulations. The authors observed that the concentration of small particles was higher in the lowest side of the reactor, since these entered the bed interior moving through the larger particles. The fraction with the smallest size was found to accumulate on the bed surface. The reactor diameter and the particle size distribution had a significant influence on this effect. Russo et al. [20] studied the influence of particle size (with particle diameter < 1 mm) on biomass pyrolysis in a channel flow at low Reynolds numbers by means of a direct numerical simulation (DNS). They found that the conversion time delay was proportional to a certain power of the particle diameter depending on the volume fraction. Caposciutti et al. [21] studied the effect of particle size (10 to 25 mm diameter) on the pyrolysis of a single wood spherical particle behavior, by monitoring its temperature, shape variation, and mass loss. They found that larger fuel particles had a milder mass loss and shape variation (as a function of time) due to a more gradual biomass heating.

Therefore, biomass size is a fundamental parameter affecting the combustion behavior. However, most of the above studies refer to laboratory scale systems, sometimes with single particles. Indeed, the combustion behavior of a fuel bed with particle sizes, which are representative of practical applications (e.g. the equivalent diameter of woodchips usually ranges from 3 to 60 mm), was seldom investigated in the literature.

In a recent study by the authors the effect of primary and secondary air distribution on the performance of a 140 kW fuel bed boiler of the underfeed stoker type was studied by using Computational Fluid Dynamics (CFD) and treating the biomass bed as a porous domain [22]. Although the numerical predictions were strongly affected by the assumption on the bed porosity, the comparison of results with the experimental flue gas composition was encouraging. Logically, a further characterization of the fuel bed would provide significant improvements.

The present study is aimed at experimentally investigating the impact of the fuel size on poplar woodchips combustion in the same 140kW underfeed stoker boiler. In particular, the temperature and the composition of the produced gases were monitored in different locations over the combustion bed, with the purpose of predicting the early and the final combustion stage behavior. The experimental data may be used for validating and/or aiding the development of numerical models of small-scale biomass combustion devices.

2. Material and methods

2.1. The experimental system

A 140 kW underfeed stoker boiler by Standard Kessel Italiana s.r.l., located at the Biomass to Energy Research Centre (CRIBE) in San Piero a Grado (Pisa, Italy), was employed in this research (Figure 1). The fuel was fed by means of a screw conveyor, with outer and inner diameter of 80 mm and 40 mm, respectively, and a pitch of 80 mm. The combustion bed is of the fixed type and has the shape of a parallelepiped with a length of 600 mm, a width of 150 mm and a height of 200 mm (Figure 2). The woodchips enter the combustion chamber from the bottom of one of the shorter sides the bed, and during the combustion process they pass through the bed longitudinally up to the opposite side of the bed. Both primary and secondary air were provided by a 2.2 kW centrifugal blower. The primary air was distributed by means of 68 rectangular nozzles (20 mm x 3 mm) placed laterally underneath the fuel bed surface. The secondary air was fed through 7 circular ducts above the fixed bed surface. Downstream of the fuel bed, a large region of the boiler is dedicated to ash collection; this region also ensures a long flue gas residence time. A gas-to-oil heat exchanger is placed above

99 the ash collection area, to transfer the exhaust gas heat to a Seriola 1510 diathermic oil, used for steam
100 generation. A suction blower is used to keep the combustion chamber pressure 20 Pa below the atmospheric
101 pressure to avoid any exhaust gas leakage in the laboratory space.

102 A thermal probe is placed upstream of the gas-to-oil heat exchanger to measure the exhaust gas
103 temperature. The probe sensitive head was properly positioned to be shielded from the direct flame
104 exposure and was equipped with a steel cap to limit the radiative loss towards the heat exchanger colder
105 regions.

106 The composition of volatiles was measured in different locations above the fuel bed by using a sampling
107 probe consisting of an L-shaped steel circular duct with an inner diameter of 6 mm. The probe is able to
108 rotate and translate along its axis in order to explore the whole bed surface while keeping the sampling point
109 always very close to the combustion bed (Figure 1b). Further details on the boiler structure, the sampling
110 probes and their sizes are reported in a previous study [14].

111

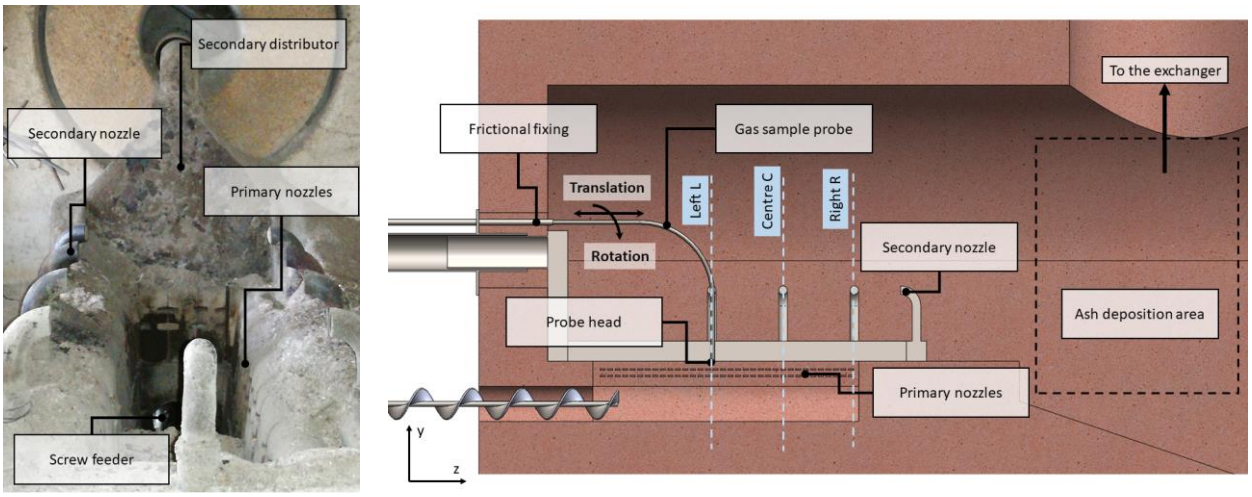

(a) *(b)*

112 *Figure 1: Details of the fire pit (a) and Scheme of the fixed bed, injection and sampling systems (b)*

113

114 Six sampling positions were selected in correspondence of the longitudinal coordinates of the secondary air
115 injection nozzles. The sampling points will hereafter be denoted by two letters, the first of them indicating

116 the position along the bed symmetry line, namely Left (L), Centre (C) and Right (R), and the second the
117 position on the bed width, namely in the Middle (M) and on the Side(s) (Figure 1). The side points are 20 mm
118 far from the primary air lateral nozzles.

119 The gas sampling probe was connected to a Watson Marlow 323S volumetric pump to fill a 0.5L Tedlar bag
120 with the gas at 0.1 L/min flow rate. The gas transfer line was equipped with a tar condensation system to
121 avoid pipeline clogging. The gas composition was analysed by means of an Agilent 3000 micro-gas
122 chromatograph (GC). The micro-GC was equipped with two independent channels both featuring an injector,
123 a column and a thermal-conductivity detector (TCD). These channels were able to measure hydrogen,
124 oxygen, nitrogen, methane, carbon monoxide, carbon dioxide, ethane, ethylene and acetylene contained in
125 the sampled gas. The GC analysis time is 3 minutes.

126 The flue gas composition was analysed downstream of the oil heat exchanger by means of an additional
127 sampling probe connected to an Environnement test bench through a line heated at 190°C. The test bench
128 included a Non-Dispersive InfraRed (NDIR) sensor, a paramagnetic sensor, and a Heated Flame Ionization
129 Detector (HFID), for the measure respectively of carbon monoxide and dioxide, oxygen, and total
130 hydrocarbons (THC) in the flue gas.

131 The temperature of the combustion bed was measured in twelve points with K-type thermocouples (TC). Six
132 of them were placed on the fuel bed surface in the same points used for gas sampling, as above described.
133 The other six thermocouples measured the temperature 100 mm below and 150 mm above the fuel bed
134 surface respectively, on the middle line points. These temperature values were labelled as T_{ij}, where i = L,C,R
135 (i.e. Left, Centre or Right longitudinal position), and j = U,M,S,L (i.e. Upper, Middle, Side or Lower line). Figure
136 2 summarizes the positions of the sampling points for both temperatures and chemical species.

137

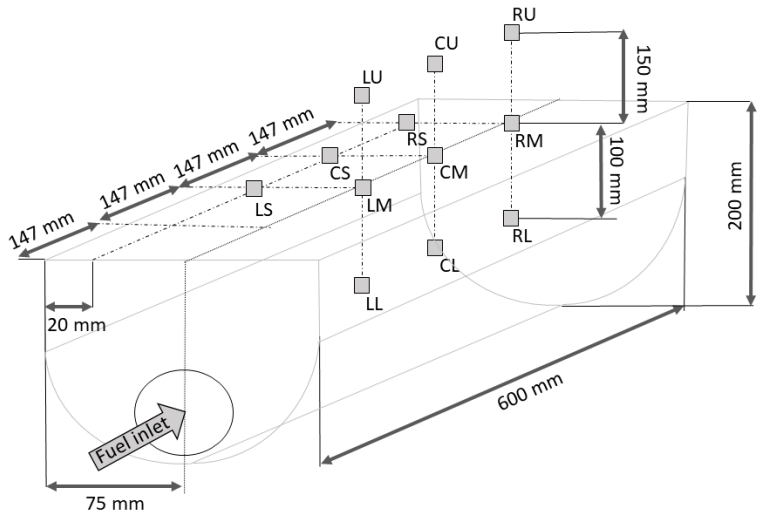

138

139 *Figure 2: Fixed bed sampling positions and main dimensions*

140 Furthermore, additional thermocouples were employed to monitor the temperatures of flue gas and
141 diathermic oil for safety reasons. Two flow speed sensors TFLOW T112 were used to measure the air flow
142 rate in the primary ($m_{a,p}$) and secondary ($m_{a,s}$) ducts, respectively.

143 The temperatures and flow rates were acquired by means of a NI 9188 chassis, equipped with NI-DAQ 9207
144 and NI-DAQ 9214 modules, and LabView software. Experimental data were further elaborated through a
145 Matlab® script.

146 The main features, measurement range and errors of the above instruments are summarized in Table 1. The
147 scheme of the experimental set-up is shown in Figure 3.

148 *Table 1: Employed instrument Features*

Instrument	Sensor	Measure	Range	Error
Environnement SA	NDIR	CO/CO_2	0 to 5000 ppm_v / 0 to 16%$_v$	<2%FS
	Paramagnetic	O_2	0 to 25%$_v$	<2%FS
	HFID	THC	0 to 30000 ppm_v	10 ppm_v
micro GC	TCD	$CO/CH_4/H_2/N_2/O_2$	0 to 100%$_v$	<1%FS
	TCD	$CO_2/C_2H_4/C_2H_6/C_2H_2$	0 to 100%$_v$	<1%FS

NI-Boards	K-type TC	Temperature	0 to 1350 °C	0.0075 T
	TFLOW T112	flow speed	0 to 30 m/s	<2.5%FS

*FS = Full Scale value

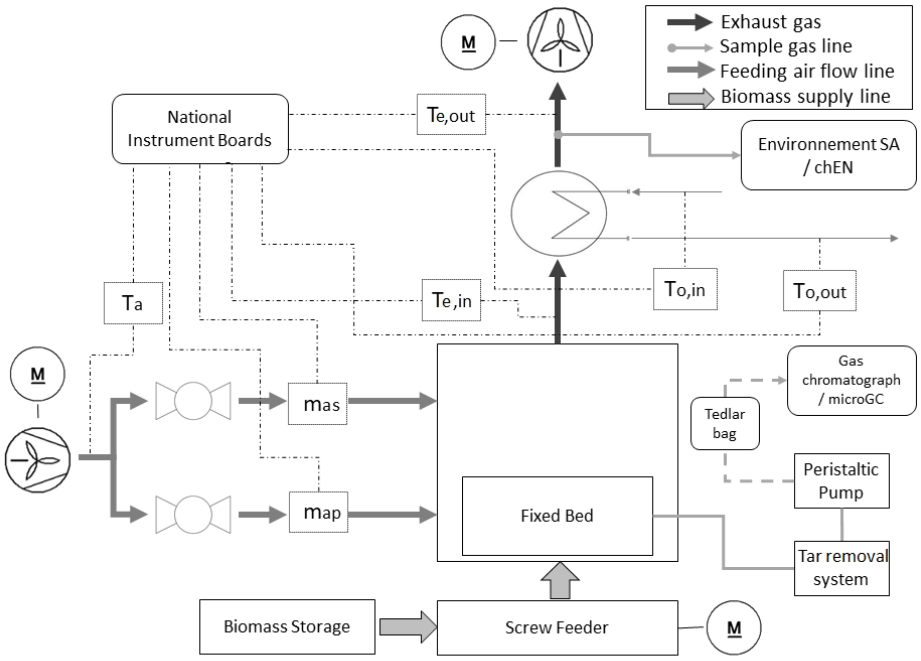

Figure 3: Scheme of experimental set-up

2.2. Fuel characteristics

The biomass employed was Poplar woodchips coming from 3-years short rotation forestry (SRF) available in the immediate surroundings of the CRIBE facility. The fuel was dried by means of a propane fired biomass drying system, thus achieving a moisture lower than 7%ar. The biomass was further characterized by the ultimate and proximate analysis (Table 2).

Table 2: Ultimate and proximate analysis for the Poplar woodchip SRF fuel

C	H	O	N	VM	FC	Ash	LHV	Moisture
[$\%_{daf}$]	[$\%_{daf}$]	[$\%_{daf}$]	[$\%_{daf}$]	[$\%_{db}$]	[$\%_{db}$]	[$\%_{db}$]	[MJ/kg_{db}]	[$\%_{ar}$]
49.01	5.83	44.59	0.57	82.46	15.35	2.19	18.38	7.0*

VM = Volatile Matter, FC = Fixed Carbon, LHV = Lower Heating Value

* After drying process

159 The biomass was firstly chipped by an on-field grinder with a size distribution identified as the coarse size.
160 The fine size was obtained by further milling the woodchips with a 5 kW NEGRI R95BHHP65 grinder. The final
161 size was then obtained by mixing the coarse and the fine woodchips in 1:1 mass ratio. The dimensional
162 distribution of each prepared fuel was measured according to the EN ISO 17827-1:2016 norm and is reported
163 in Figure 4.
164 The dimensional distributions were characterized using the Sauter mean diameter (SMD) and the mass
165 median diameter (MMD). The SMD was estimated as:

166 $$\mathrm{SMD} = \frac{\sum_1^N f_{n,i} {d_i}^3}{\sum_1^N f_{n,i} {d_i}^2} = \frac{1}{\sum_1^N \frac{f_i}{d_i}} \quad (1)$$

167 Where $f_{n,I}$ and f_i are the numerical and mass fractions, respectively, of the i-th size bin, i.e. with d_i being its
168 characteristic diameter [23,24]. The f_i is basically the one reported in Figure 4.
169 The MMD represents the diameter corresponding to a mass cumulative frequency of 50%$_{wt}$. The fuel bulk
170 density was also evaluated according to the EN ISO 18847:2016 norm. For all the employed fuel sizes the bulk
171 density, SMD, MMD, and maximum diameter are reported in Table 3.
172

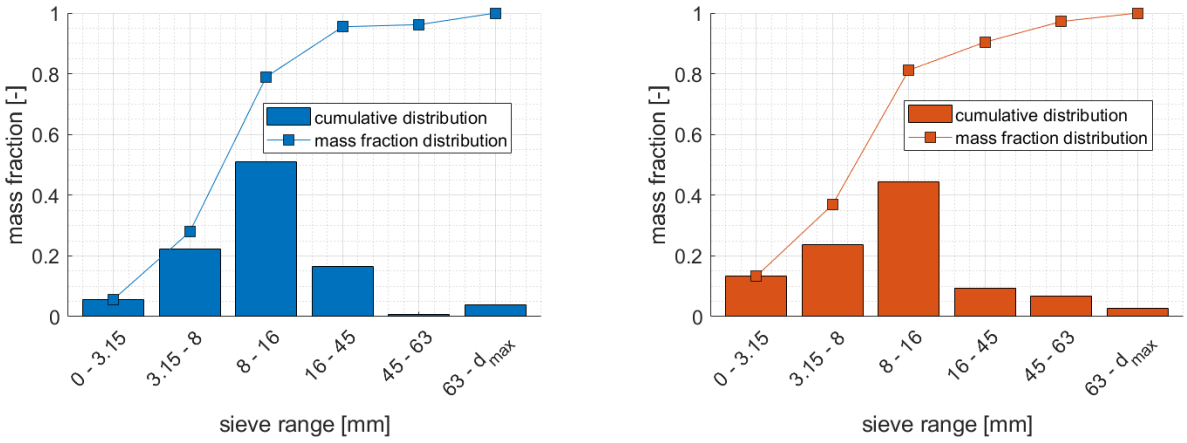

(a) *(b)*

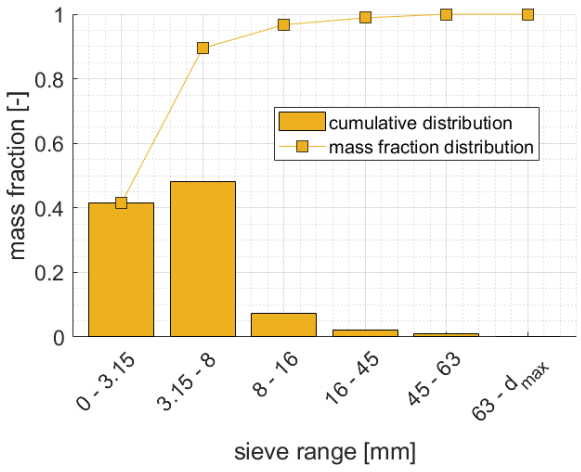

(c)

Figure 4: Size distribution for coarse (a), mix (b) and fine (c) size fuels

173

174 *Table 3: Characterization of the dimensional distribution for the three fuel sizes.*

Size	Bulk density [kg_{ar}/m^3]	MMD [mm]	SMD [mm]	d_{max} [mm]
Coarse	147	8.1	8.0	85
Mix	152	7.3	5.9	87
Fine	162	2.2	2.8	61

175

176 Figure 5 shows how both the MMD and the SMD decrease with the bulk density. The SMD shows a nearly
177 linear relation with the bulk density, and was then employed as size indicator to compare the performance
178 of the three fuel sizes.

179 In order to account for moisture content variation due to the high biomass hygroscopicity, the analysis of
180 fuel moisture was repeated immediately before the experimental tests, obtaining 9.3%$_{ar}$, 10.2%$_{ar}$ and 9.5%$_{ar}$
181 for the coarse, mix and fine woodchips, respectively.

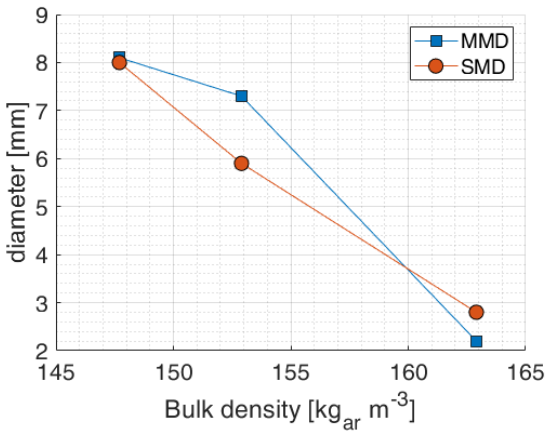

Figure 5: SMD and MMD as functions of the bulk density

2.3. Test method

The boiler operating conditions were described through the air split ratio λ and the excess air ε. The former represents the secondary to primary mass flow rate ratio [14,25]:

$$\lambda = \frac{m_{a,s}}{m_{a,p}} \quad (5)$$

where $m_{a,s}$ and $m_{a,p}$ are the secondary and primary air mass flow rates, respectively.

The excess air ε is defined as:

$$\varepsilon = \frac{\alpha - \alpha_{st}}{\alpha_{st}} \quad (2)$$

where α indicates the feed air to biomass mass flow rate ratio and α_{st} represents its stoichiometric value. According to the complete combustion reactions pathways, the stoichiometric air to fuel ratio can be calculated using the fuel composition in dry ash free basis units $Y_{i,f}^{daf}$:

$$\alpha_{st} = 11.5\, Y_{C,f}^{daf} + 34.48 Y_{H,f}^{daf} + 4.31 Y_{S,f}^{daf} + 9.85 Y_{N,f}^{daf} - 4.31 Y_{O,f}^{daf} \quad (3)$$

Therefore, Equation 2 can be re-arranged by means of the flue gas oxygen mass fraction Y_{O2} as [14,25]:

$$\varepsilon = \frac{4.31\, Y_{O2} + \alpha_{st}}{\alpha_{st}\,(1 - 4.31\, Y_{O2})} - 1 \quad (4)$$

The excess air was monitored by measuring the oxygen content in the flue gas, which was controlled by varying the air blower speed. On the other hand, the air split ratio was controlled by acting on the sphere valves placed on the air supply manifolds. The variation range of both λ and ε was limited by the blower

200 capabilities and the combustion process stability. For each fuel size six tests were performed corresponding
201 to the nominal conditions reported in Table 4.

202 *Table 4: Nominal values of excess air and air split ratio for each test denoted with an ID number.*

		ε [-]	
		2	1.5
λ [-]	1	ID1	ID4
	0.5	ID2	ID5
	0.1	ID3	ID6

203

204 The composition of volatiles was referred to the total content of volatiles in the gas phase, by calculating the
205 mass fraction of the i-th component in the biomass volatiles as:

206 $$Y_{i,vol} = \frac{Y_{i,wt}}{\sum_{i=1}^{N,vol} Y_{i,wt}} \quad (6)$$

207 Where $Y_{i,wt}$ is the mass fraction of the i-th volatile component measured in the gas by the GC. Specifically, the
208 considered components were CO, CO_2, H_2, CH_4, C_2H_2, C_2H_4 and C_2H_6 [26].

209 The biomass mass flow rate was about 16 kg/h for all the reported cases. Each operational condition was
210 maintained for at least 30 minutes in order to collect a statistically meaningful number of data. Indeed, the
211 temperatures and the flue gas species concentrations were represented by using a time-average and a
212 standard deviation σ of the measured values over the sampling time. The chemical species sampling on the
213 fuel bed was carried out for 5 minutes (i.e. time to fill a Tedlar bag). The reported concentrations were
214 therefore calculated as the average over 5 minutes of experimental run.

215 The correlation between volatiles and the SMD was estimated by means of two coefficients:

216 1. The first was the Pearson coefficient R [27], calculated between the mass fractions of the i-th species
217 in volatiles ${Y^j}_{i,vol}$ and the SMD , as:

218 $$R_i = \frac{\sum_{j=1}^{N}\left({Y^j}_{i,vol} - \overline{Y_{i,vol}}\right)\left(SMD^j - \overline{SMD}\right)}{\sqrt{\sum_{j=1}^{N}\left({Y^j}_{i,vol} - \overline{Y_{i,vol}}\right)^2}\ \sqrt{\sum_{j=1}^{N}\left(SMD^j - \overline{SMD}\right)^2}} \quad (7)$$

The $\overline{Y_{i,vol}}$ and the $\overline{SMD}$ are the averages of the $Y_{i,vol}$ and SMD data series, respectively.

2. The second coefficient was $\hat{m}$ (i.e. the derivative parameter), which was adopted to evaluate the percentage variation of $Y_{i,vol}$ with respect to the SMD variation as:

$$\hat{\mathrm{m}} = \frac{\partial\, \mathrm{Y_{i,vol}}}{\partial\, \mathrm{SMD}} \left.\frac{100}{\max(\Delta \mathrm{Y_{i,vol}})}\right|_{\text{linear fitting}} \quad (8)$$

In the above equation, the derivative is estimated from the slope of the best linear fitting.

3. Results and Discussion

The measured operating conditions obtained for the experimental tests are reported in Table 5.

Table 5: Actual values of operating conditions

	coarse size			mix size			fine size		
	ε [-]	λ [-]	$m_{a,tot}$ [kg/s]	ε [-]	λ [-]	$m_{a,tot}$ [kg/s]	ε [-]	λ [-]	$m_{a,tot}$ [kg/s]
ID1	2.09±0.06	0.7±0.5	0.09±0.05	2.80±0.03	0.99±0.04	0.087±0.002	1.91±0.02	1.05±0.09	0.085±0.005
ID2	2.67±0.04	0.6±0.2	0.10±0.02	2.59±0.06	0.51±0.03	0.085±0.004	1.91±0.05	0.52±0.02	0.091±0.002
ID3	2.40±0.06	0.2±0.2	0.06±0.06	2.22±0.05	0.108±0.003	0.097±0.002	1.83±0.03	0.109±0.003	0.096±0.002
ID4	1.39±0.05	0.7±0.5	0.05±0.03	1.76±0.05	0.99±0.05	0.054±0.002	1.73±0.05	0.97±0.06	0.050±0.002
ID5	1.74±0.04	0.6±0.2	0.05±0.01	1.80±0.06	0.48±0.03	0.054±0.003	1.37±0.03	0.51±0.05	0.052±0.004
ID6	1.65±0.05	0.5±0.4	0.06±0.04	1.44±0.06	0.105±0.005	0.058±0.002	1.18±0.05	0.106±0.005	0.057±0.002

The system was able to keep the operating conditions sufficiently close to the chosen points (Table 4) in almost all the cases, except for the tests with the coarse particle size. Here, the errors on the operating conditions were significantly larger than for the other test cases. This could be partly attributed to the secondary blower PID controller tuning, which caused some oscillations in the primary and secondary air flow rates. Nevertheless, the excess air ε was only slightly affected as confirmed by the fact that error values are similar to those estimated for the mixed and fine fuel size.

3.1. Early combustion species

3.1.1. Effect of the operating conditions

Figure 6 shows the effect of λ and ε on the main gases released from early combustion in the different sampling locations (see Side and Middle lines of Figure 2) on the fuel bed surface. Data about Figure 6 are available in Table A.1 and A.2. The reported values refer to the mixed and fine particle sizes because, as mentioned before, the tests with the coarse size were characterized by different operating conditions, and this would prevent a fair comparison.

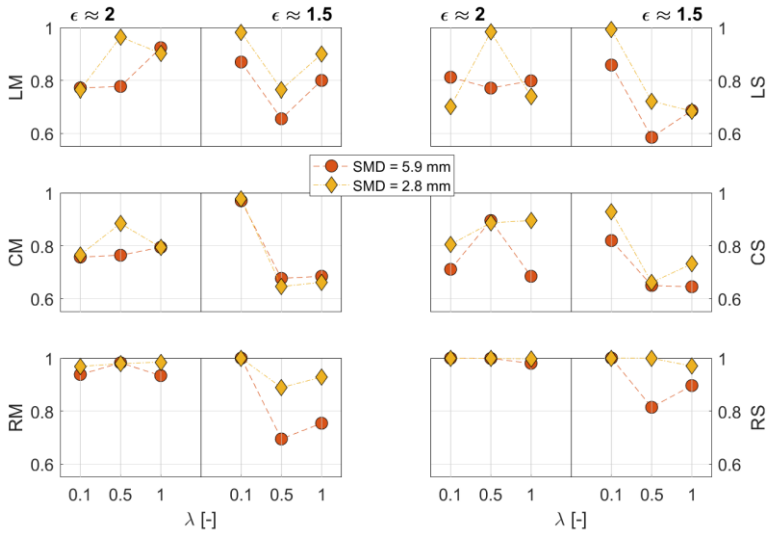

a) CO_2 [kg_i/kg_{vol}]

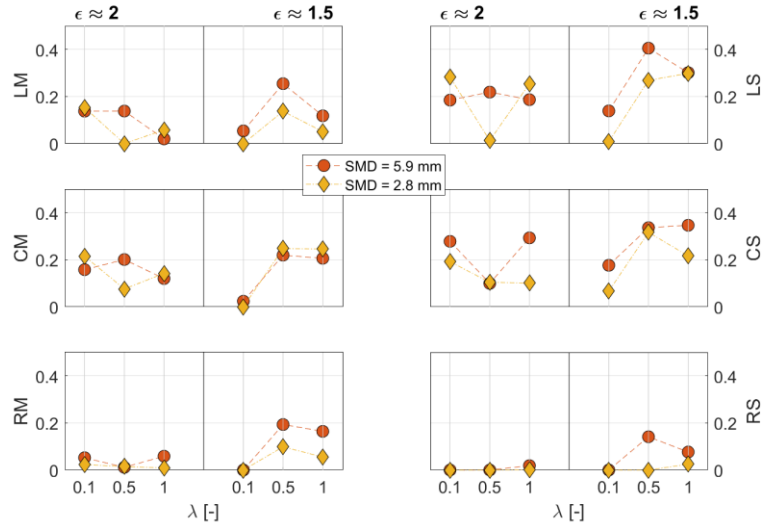

b) CO [kg_i/kg_{vol}]

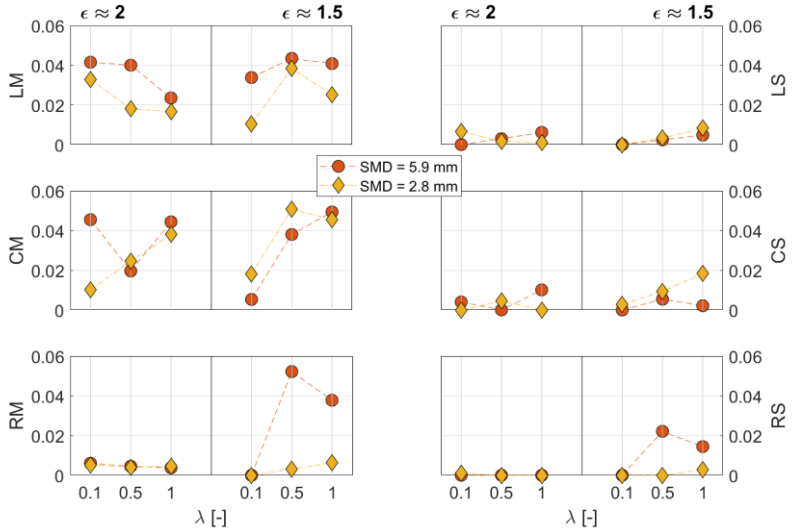

c) CH_4 [kg_i/kg_{vol}]

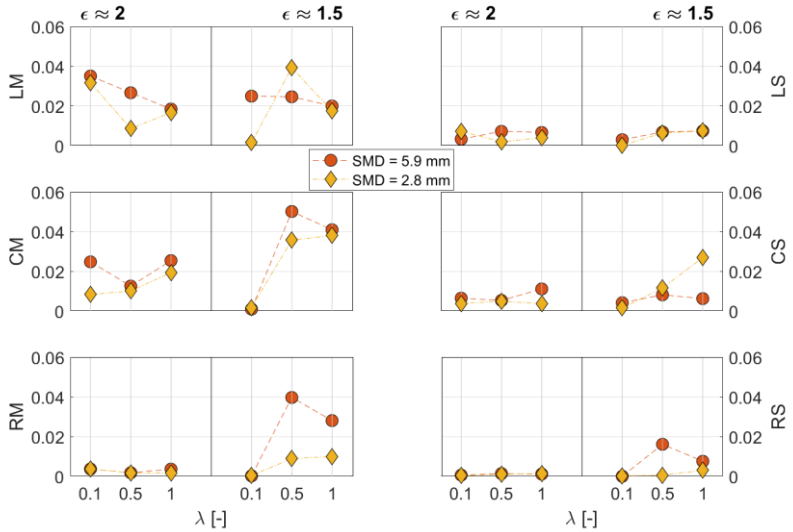

d) H_2 [kg_i/kg_{vol}]

Figure 6: Measured CO_2 (a), CO (b), CH_4 (c) and H_2 (d) as a function of λ and ε on different sampling points on the fuel bed surface

Carbon monoxide and dioxide showed similar trends in all the sampling points and with all the fuels (Figure 6 (a,b)), thus pointing out that the air split ratio λ had the same influence on both these gases. This effect was observed for both excess air values. This behavior was also in agreement with previous experimental campaigns [14]. Moreover, the concentrations of the volatile species varied strongly in space, decreasing

248 from the left (i.e. near the fuel inlet) to the right of the fire pit, and from the middle to the side sampling
249 lines.

250 Methane and hydrogen also showed a similar behavior in most of the sampling locations as shown in Figure
251 6 (c,d). However, being the concentration of these species always below 2%$_{wt,vol}$ for the RM, RS and CS
252 positions with $\varepsilon \approx 2$, a clear trend is difficult to be derived with sufficient reliability.

253 As a whole, the operating conditions affected the emission of volatiles in the same way regardless of the fuel
254 sizes. This observation suggests that it is possible to decouple the effect of the operating conditions from the
255 fuel size, at least in the range of conditions here reported. Hence, a global trend (i.e. by considering the whole
256 [λ, ε] dataset) of the concentrations of early stage volatiles can be established simply as a function of the
257 SMD.

258 **3.1.2. Effect of particle diameter**

259 The effect of particle size was analysed by averaging the values of $Y_{i,vol}$ over the operating points from ID1 to
260 ID6. Figure 7 depicts the CO, CO_2, H_2, CH_4, C_2H_4 and C_2H_6 mass concentration measured in the six points along
261 the side and middle lines on the fuel bed surface as a function of the SMD. Data about Figure 7 are available
262 in Table A.3. The acetylene was not reported here, as its concentration in the sampled gas was lower than
263 0.01 %$_{wt}$ in all the cases, in agreement with the previous findings [14].

264 The mass fraction of CO, H_2, CH_4, C_2H_4 and C_2H_6 in the volatile gases showed well defined trends, thus pointing
265 out a strong correlation between the SMD and volatiles. Particularly, the Pearson coefficient R is larger than
266 0.95 for CO, CO_2, H_2 and CH_4 (Table 6). The volatiles concentration as a function of SMD could be fitted by a
267 straight line, having a positive slope of about 19% of the total yield over a millimetre SMD variation for all
268 these species. In contrast, a negative slope is observed for the carbon dioxide; this is consistent with the fact
269 that a significant part of CO_2 comes from the oxidation of CO and hydrocarbons, thus CO_2 is inversely related
270 to the concentration of the other volatile species.

271

272 *Table 6: Pearson coefficient R and $\hat{m}$ for the early stage combustion species.*

		LM	LS	CM	CS	RM	RS
R [-]	CO	0.97	0.44	0.81	0.99	0.98	0.99
$\hat{m}$ [%$_{range}$/mm]		19	9	18	19	19	19
R [-]	CO_2	-0.98	-0.37	-0.90	-0.99	-1.00	-0.99
$\hat{m}$ [%$_{range}$/mm]		-19	-7	-18	-19	-19	-19
R [-]	CH_4	1.00	-0.92	0.87	0.18	0.91	1.00
$\hat{m}$ [%$_{range}$/mm]		19	-18	18	3	20	19
R [-]	H_2	1.00	-0.07	0.95	0.33	0.97	0.98
$\hat{m}$ [%$_{range}$/mm]		19	-1	20	6	20	19
R [-]	C_2H_4	1.00	-0.24	0.99	-0.88	0.59	0.92
$\hat{m}$ [%$_{range}$/mm]		19	-5	19	-19	11	20
R [-]	C_2H_6	0.95	-0.96	0.88	-0.17	0.92	1.00
$\hat{m}$ [%$_{range}$/mm]		19	-19	18	-4	20	19

273

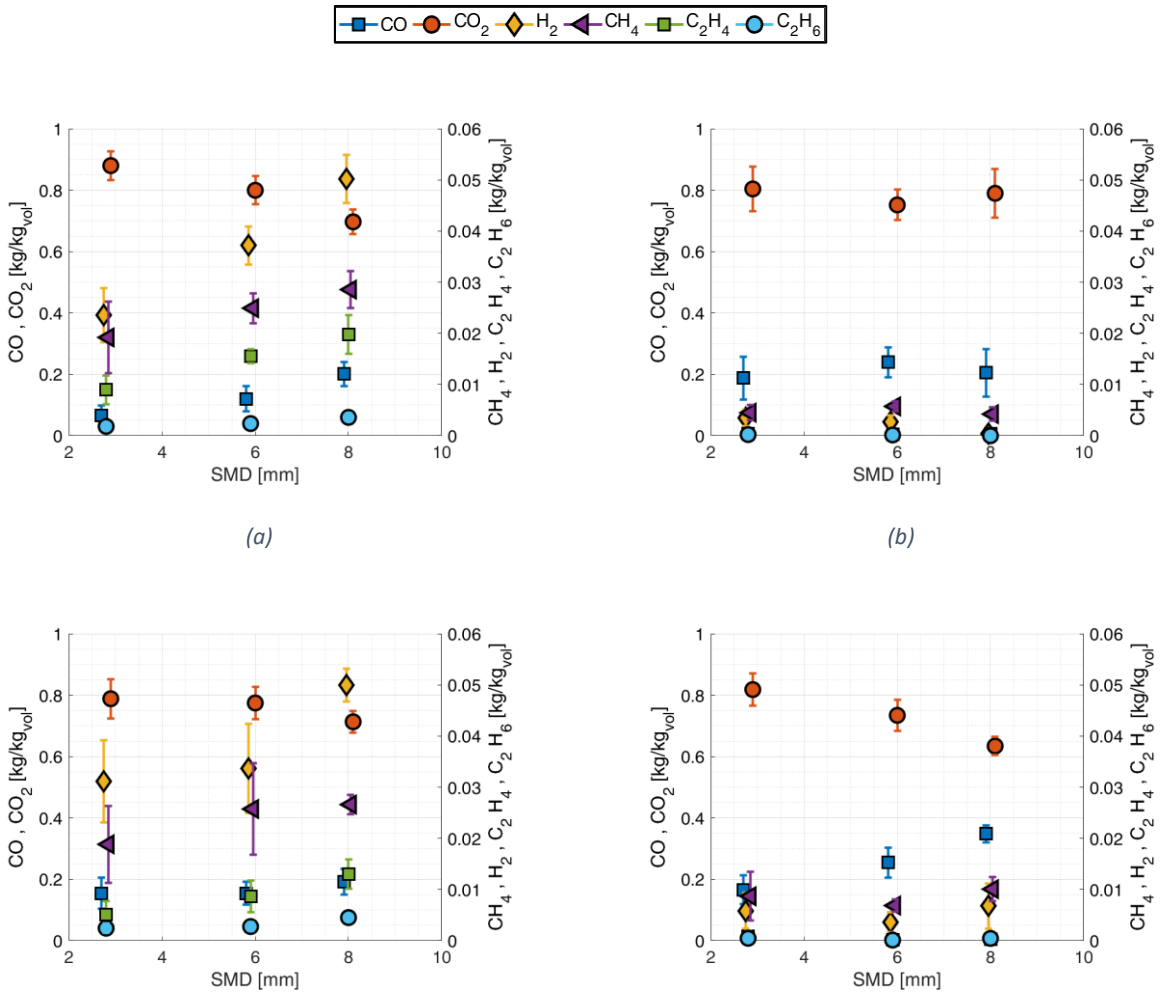

(a) *(b)*

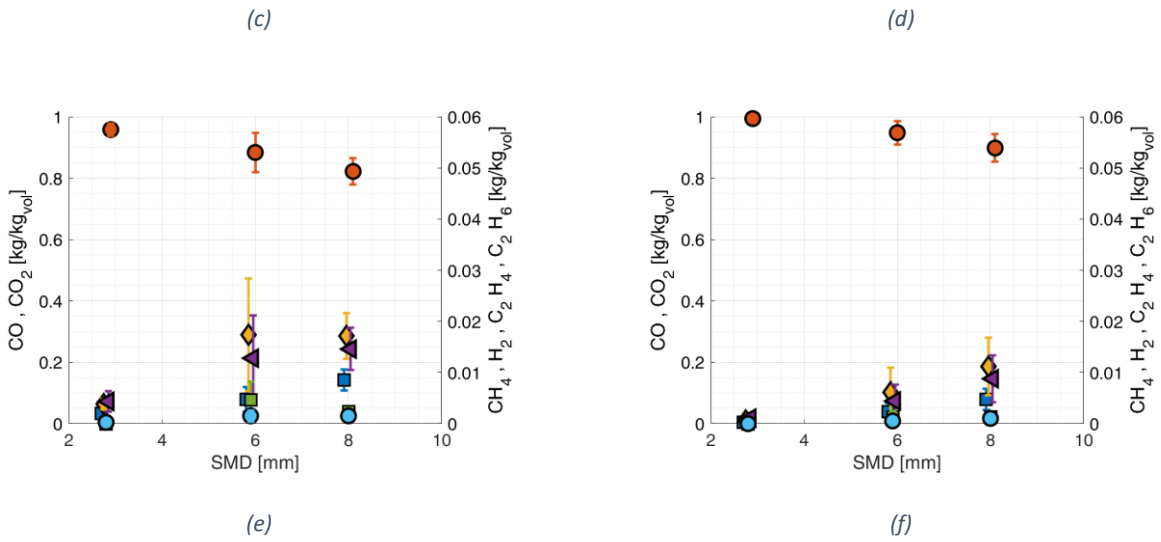

Figure 7: Volatile gas species composition for the different SMD employed in different locations: LM (a), LS (b), CM (c), CS (d), RM (e) and RS (f).

The effect of the SMD can be explained by the dependency of the fuel dimension on the particle heating rate. In particular, smaller particles undergo higher heating rates than larger particles, because of their larger area to volume ratio. Since high heating rates result in a fast release of volatiles [28,29], small fuels will likely show localized release of volatiles. As a matter of fact, the amount of released volatiles on the right side of the fire pit is nearly zero (Figure 7), thus indicating that the devolatilization has already completed. Particles with larger SMD produce a more evenly distributed volatile release due the slower heating rate with respect to smaller particles. In this case, in fact, the volatile release appears to be shifted towards the right side of the fuel bed, with the result of a larger volatile content detection.

Looking back at Table 6, low R values were observed for the LS location. In that sampling point the bed height was observed to be larger than in other sampling points, because the counter-clockwise rotation of the screw conveyor caused an accumulation of the woodchips on the left-side area of the bed. Hence, in this location the gas probe often sampled below the bed surface, thus interacting with the solid woodchips. This led to a significant aliasing of the measurements, which prevented obtaining a defined correlation between SMD and volatiles.

In all locations the volatile gas (Figure 7) was mainly composed by CO_2 (between 60 to 100%$_{wt,vol}$), CO (between 5 and 20%$_{wt,vol}$), hydrogen and methane (below of 5%$_{wt,vol}$). Ethane and ethylene concentration was

below 2%$_{wt,vol}$. These findings are in fair agreement with the work of Neves et al. [26], who estimated a CO concentration between 20 to 60%$_{wt,vol}$ and a CO_2 concentration between 20 to 80 %$_{wt,vol}$ in biomass pyrolysis experiments. The different values here found can be related to the oxidative conditions employed in the present tests. H_2 and CH_4 and the sum of other hydrocarbons measured by Neves et al. [26] are 2 to 4 times higher (i.e. their values are up to 10%$_{wt,vol}$) than those in the present investigation (i.e. up to 3%$_{wt,vol}$). Buchmayr et al. [30] reported CO in the range from 10 to 25% by volume, while H_2 and CH_4 below of 6% by volume in the primary combustion region of a small woodchip boiler; these values were close to the present measurements.

The total volatile yield in the fuel bed surface was calculated as the sum of the concentrations of CO_2, CO, H_2, CH_4, C_2H_2, C_2H_4 and C_2H_6. The total volatile yield profiles (Figure 8) confirm that devolatilization and combustion occur earlier for particles with smaller SMD because of their faster heating rate with respect to larger SMD particles. Indeed, the maximum volatile yield is observed on the left positions for SMD=2.8 mm, while in the centre or even in the right positions for SMD=8.0 mm.

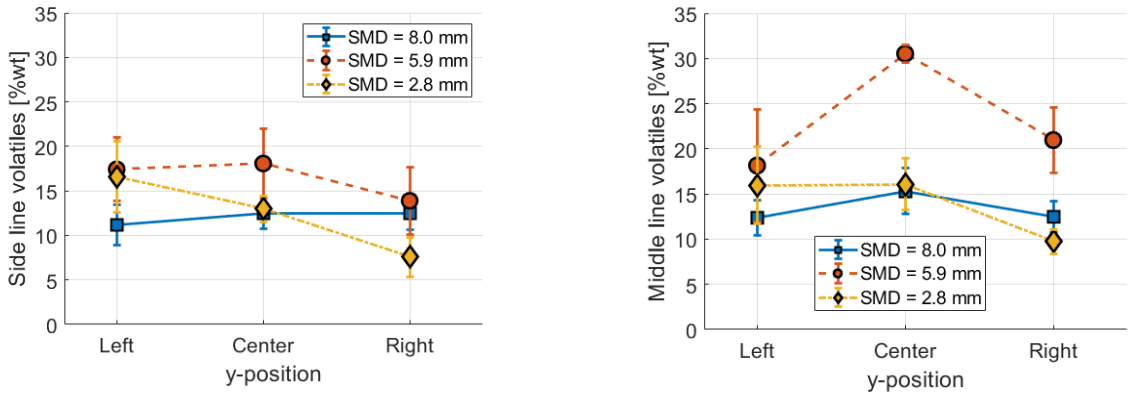

Figure 8: Profiles of volatile yield for different SMD on the (a) Side and (b) Middle lines.

The fuel with mixed size shows an interesting behavior. In particular, it is characterized by larger volatile yields than that with the other two SMDs. This finding is worthy of further investigation, but it may be partly attributed to segregation effects [19,31], leading to differential paths of small and large particles, thus affecting heating rates and ultimately their volatile release.

3.2. Fuel bed temperatures

In order to compare the effect of the fuel size on bed thermal behavior, the measured temperatures were averaged over the different operating conditions. The resulting profiles are reported in Figure 9 for the Upper, Middle, Side or Lower lines. The temperature values are not reported for the left-side (LS) positions because of an erratic behavior of the thermocouple which detected temperature spikes (above 2000 K) which could indicate a failure in the thermocouple connection. The sensor failure probability in this particular position was increased by the solid fuel accumulation caused by the counter-clockwise rotation of the screw conveyor, which led to higher mechanical stresses, with respect to the other probes.

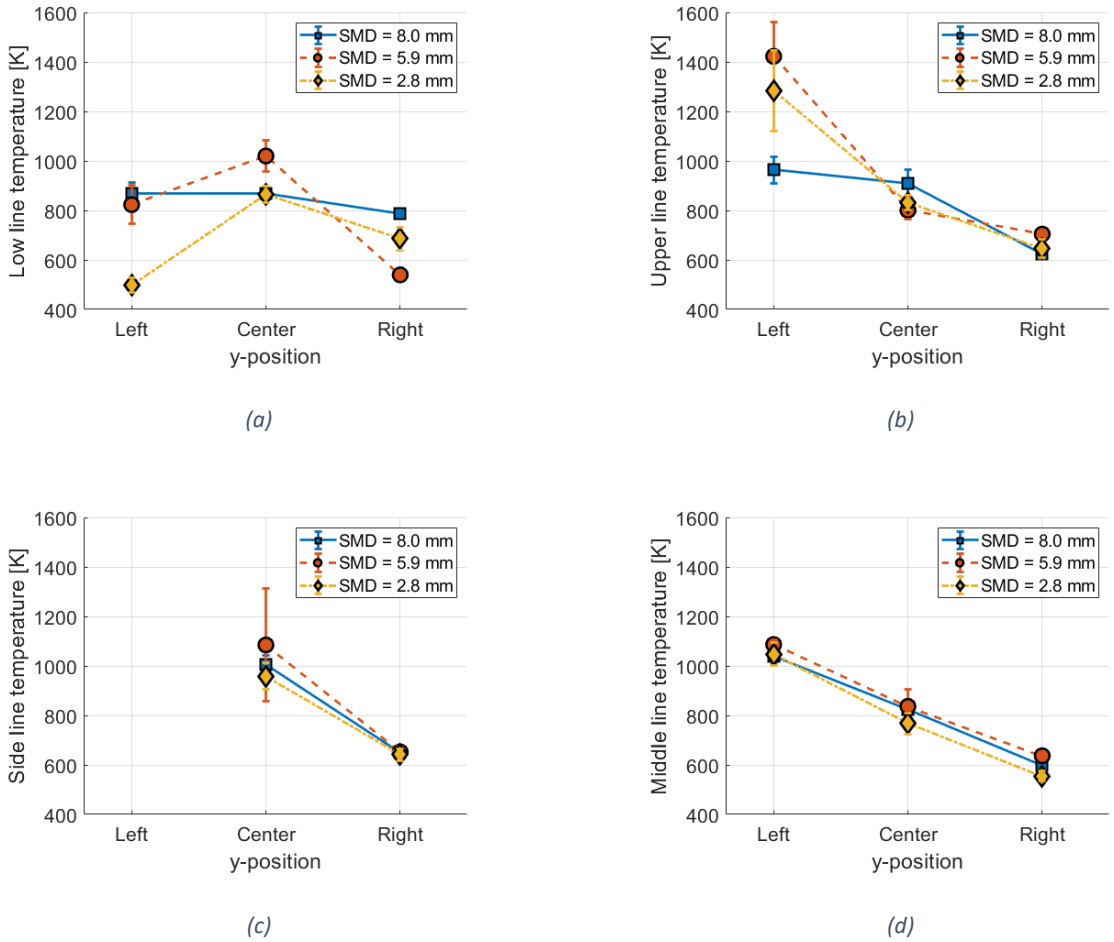

Figure 9: Averaged temperatures for the different IDs, considering the lower (a), upper (b), side (c) and middle (d) sampling lines.

The highest temperatures were measured above the fuel bed (see the Upper line) where volatile oxidation occurs. In particular, the fine and mix fuel sizes indicated temperatures of about 1300-1400 K on the left side of the fire pit, in agreement with the localized release (and consequent oxidation) of volatiles in this region.

As expected, the lowest temperatures were measured underneath the fuel bed surface (see the Lower line) because of the negligible direct exposure to flame radiation. Measurements indicate a large spatial variation of temperature, especially for the fine and mixed size fuels, while a fairly constant trend was observed for the coarse size fuel. The explanation of this different thermal behavior would require a better comprehension of the fuel bed motion, reaction and heat transfer, eventually including segregation phenomena.

The bed surface temperature (see Side and Middle lines in to Figure 9 (c,d)) shows a small effect of the SMD and an almost linear monotonic decrease of temperatures from the left to the right side of the fire pit. In particular, in the right position, the fuel bed temperatures are relatively low for all SMDs (about 600 K).

3.3. Carbon monoxide, carbon dioxide emissions and flue gas temperature

The CO and CO_2 concentrations in the flue gases are reported in Figure 10, along with the flue gas temperature upstream of the gas-to-oil heat exchanger. The THC content is not reported as it was always very low, i.e. lower than 10 ppmv. In the graphs in Figure 10, the hollow points represent all the experiments, whereas the solid circles correspond to the values averaged over the different operating conditions.

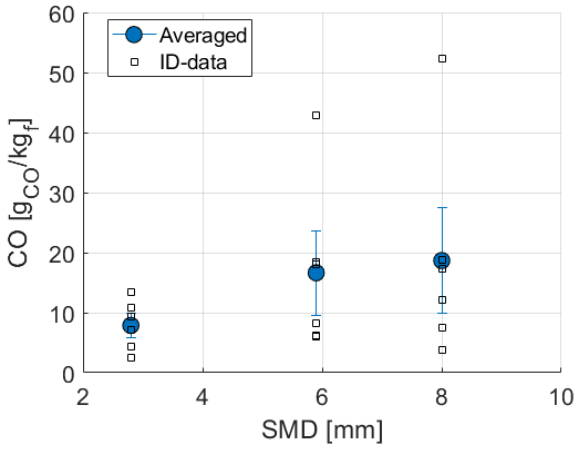

(a)

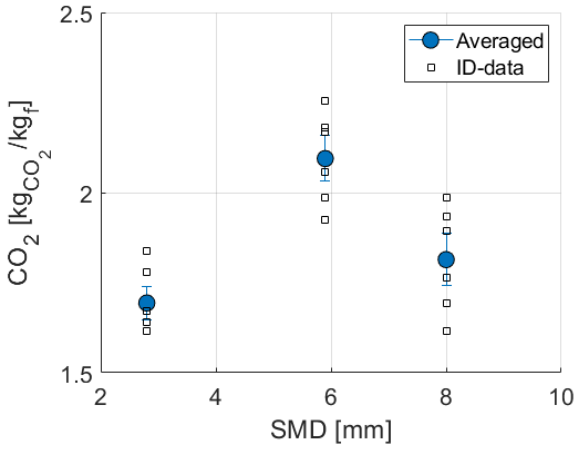

(b)

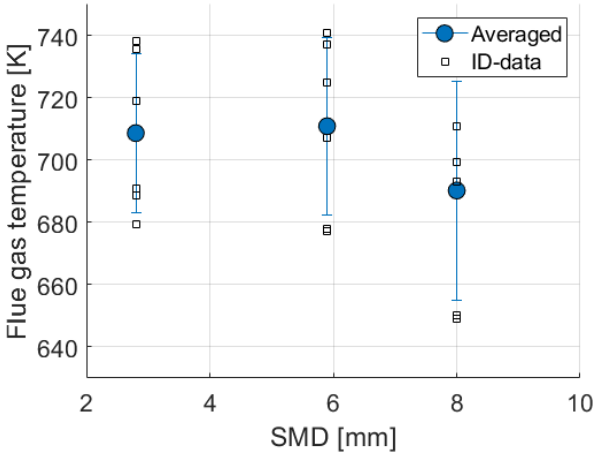

(c)

Figure 10: Exhaust gas CO (a) and CO_2 (b) content, together with exchanger inlet temperature (c), as a function of the SMD

The carbon monoxide emissions were mainly between 2 and 20 g/kg_f, with peaks of 50 g/kg_f observed for the coarse size fuel. The carbon dioxide emissions were between 1.5 and 2.3 g/kg_f and flue gas temperatures $T_{e,in}$ between 650 and 740 K.

The wide scatter of data, especially for CO concentration, hinders possible correlations between the fuel size in one hand and CO, CO_2 and temperatures in the other. However, CO increases with SMD, with a minimum of 10 g/kg_f obtained for the fine size, i.e. SMD = 2.8 mm, thus indicating the best combustion behavior of small woodchips. CO_2 concentration presents a maximum for the mixed fuel type, thus confirming, again, that the mixed fuel behavior cannot be predicted by simply averaging the results for fine and coarse size fuels.

4. Conclusions

The effect of fuel size on the combustion of woodchips in a small boiler was investigated by sampling the concentration of volatile species at different locations on the fuel bed surface and by monitoring temperatures inside, above and on the surface of the fuel bed. The fuel size was found to have a significant impact on the release profiles of the early stage combustion gases. Coarse particles resulted in a nearly

uniform volatile distribution above the fire pit, while fine particles caused a localized emission of volatiles, which occurred very close to the feeding. This could be explained with the fast heating rate of small particles that have a large surface to volume ratio. Moreover, linear correlations between the concentration of volatiles and the SMD were observed for all the investigated volatile species. The mixed size fuel, obtained by mixing fine and coarse woodchips, exhibited the largest total volatile yield. In addition, the species concentration and the temperature measured with the mixed size were only seldom in between those found with the fine and coarse particles. This suggests that the combustion behavior of a fuel obtained by mixing two fuels with different particle sizes cannot be predicted by simply averaging the behaviors of the single fuels. Other effects, such as fuel segregation, can play a key role as fine and coarse particles may undergo different pathways and thus experience different heating rates, ultimately affecting volatile release and combustion. As for the flue gases, a minor influence of the fuel size on the species concentrations and temperatures was observed, at least in the employed operating conditions.

The present dataset may be valuable for the validation of numerical models, based on computational fluid dynamics, of small biomass boilers. In particular, the large spatial variation of chemical species and temperature on the fire pit surface, suggests that zero-dimensional models of the fuel bed are unsuited and thus care should be taken when using freeboard-only approaches. On the other hand, the peculiar behavior of the mix sized fuel indicates the importance of segregation phenomena which could be accounted by coupling computational fluid dynamics with models for granular flows, such as discrete element methods.

References

[1] H. Long, X. Li, H. Wang, J. Jia, Biomass resources and their bioenergy potential estimation: A review, Renew. Sustain. Energy Rev. 26 (2013) 344–352. doi:https://doi.org/10.1016/j.rser.2013.05.035.

[2] I. Batas-Bjelic, N. Rajakovic, N. Duic, Smart municipal energy grid within electricity market, Energy. 137 (2017) 1277-1285. doi:http://dx.doi.org/10.1016/j.energy.2017.06.177.

[3] I. Dincer, C. Acar, Smart energy systems for a sustainable future, Appl. Energy. 194 (2017) 225–235.

373 doi:http://dx.doi.org/10.1016/j.apenergy.2016.12.058.

374 [4] R. Ruan, P. Chen, R. Hemmingsen, R. Morey, D. Tiffany, Size matters: Small distributed biomass
375 energy production systems for economic viability, Int. J. Agric. Biol. Eng. 1 (2008) 64–68.
376 doi:10.3965/j.issn.1934-6344.2008.01.064-068.

377 [5] A.A. Zabaniotou, V.K. Skoulou, D.P. Mertzis, G.S. Koufodimos, Z.C. Samaras, Mobile Gasification
378 Units for Sustainable Electricity Production in Rural Areas: The SMARt-CHP Project, Ind. Eng. Chem.
379 Res. 50 (2011) 602–608. doi:10.1021/ie100202p.

380 [6] D.S. Bajwa, T. Peterson, N. Sharma, J. Shojaeiarani, S.G. Bajwa, A review of densified solid biomass
381 for energy production, Renew. Sustain. Energy Rev. 96 (2018) 296–305.
382 doi:https://doi.org/10.1016/j.rser.2018.07.040.

383 [7] S.A. Mehetre, N.L. Panwar, D. Sharma, H. Kumar, Improved biomass cookstoves for sustainable
384 development: A review, Renew. Sustain. Energy Rev. 73 (2017) 672–687.
385 doi:https://doi.org/10.1016/j.rser.2017.01.150.

386 [8] European Commission, Sustainable and optimal use of biomass for energy in the EU beyond 2020.,
387 (2017) 170. https://ec.europa.eu/energy/sites/ener/files/documents/biosustain_report_final.pdf
388 (accessed July 26, 2019).

389 [9] J.P. Carroll, J.M. Finnan, F. Biedermann, T. Brunner, I. Obernberger, Air staging to reduce emissions
390 from energy crop combustion in small scale applications, Fuel. 155 (2015) 37–43.
391 doi:10.1016/j.fuel.2015.04.008.

392 [10] M. Buchmayr, J. Gruber, M. Hargassner, C. Hochenauer, Performance analysis of a steady flamelet
393 model for the use in small-scale biomass combustion under extreme air-staged conditions, J. Energy
394 Inst. 91 (2018) 534–548. doi:10.1016/j.joei.2017.04.003.

395 [11] H. Khodaei, F. Guzzomi, G.H. Yeoh, A. Regueiro, D. Patiño, An experimental study into the effect of
396 air staging distribution and position on emissions in a laboratory scale biomass combustor, Energy.

118 (2017) 1243–1255. doi:10.1016/j.energy.2016.11.008.

[12] H. Khodaei, F. Guzzomi, D. Patiño, B. Rashidian, G.H. Yeoh, Air staging strategies in biomass combustion-gaseous and particulate emission reduction potentials, Fuel Process. Technol. 157 (2017) 29–41. doi:10.1016/j.fuproc.2016.11.007.

[13] M. Buchmayr, J. Gruber, M. Hargassner, C. Hochenauer, Experimental investigation of the primary combustion zone during staged combustion of wood-chips in a commercial small-scale boiler, Biomass and Bioenergy. 81 (2015) 356–363. doi:http://dx.doi.org/10.1016/j.biombioe.2015.07.016.

[14] G. Caposciutti, F. Barontini, M. Antonelli, L. Tognotti, U. Desideri, Experimental investigation on the air excess and air displacement influence on early stage and complete combustion gaseous emissions of a small scale fixed bed biomass boiler, Appl. Energy. 216 (2018) 576–587. doi:https://doi.org/10.1016/j.apenergy.2018.02.125.

[15] K.M. Bryden, M.J. Hagge, Modeling the combined impact of moisture and char shrinkage on the pyrolysis of a biomass particle, Fuel. 82 (2003) 1633–1644. doi:https://doi.org/10.1016/S0016-2361(03)00108-X.

[16] P. Holmgren, D.R. Wagner, A. Strandberg, R. Molinder, H. Wiinikka, K. Umeki, M. Broström, Size, shape, and density changes of biomass particles during rapid devolatilization, Fuel. 206 (2017) 342–351. doi:https://doi.org/10.1016/j.fuel.2017.06.009.

[17] M. Bellais, K.O. Davidsson, T. Liliedahl, K. Sjöström, J.B.C. Pettersson, Pyrolysis of large wood particles: a study of shrinkage importance in simulations, Fuel. 82 (2003) 1541–1548. doi:https://doi.org/10.1016/S0016-2361(03)00062-0.

[18] H. Lu, E. Ip, J. Scott, P. Foster, M. Vickers, L.L. Baxter, Effects of particle shape and size on devolatilization of biomass particle, Fuel. 89 (2010) 1156–1168. doi:https://doi.org/10.1016/j.fuel.2008.10.023.

[19] X. Liu, Q. Chen, Y. Xi, C. You, Segregation of multi-sized biomass particles in a horizontal stirred bed,

421 Powder Technology 303 (2016) 130–137. doi.org/10.1016/j.powtec.2016.09.024.

422 [20] E. Russo, J.G.M. Kuerten, B.J. Geurts, Delay of biomass pyrolysis by gas-particle interaction, J. Anal.
423 Appl. Pyrolysis. 110 (2014) 88–99. doi:10.1016/j.jaap.2014.08.011.

424 [21] G. Caposciutti, H. Almuina-Villar, A. Dieguez-Alonso, T. Gruber, J. Kelz, U. Desideri, C. Hochenauer, R.
425 Scharler, A. Anca-Couce, Experimental investigation on biomass shrinking and swelling behaviour:
426 Particles pyrolysis and wood logs combustion, Biomass and Bioenergy. 123 (2019) 1–13.
427 doi:https://doi.org/10.1016/j.biombioe.2019.01.044.

428 [22] S. Patronelli, M. Antonelli, L. Tognotti, C. Galletti, Combustion of wood-chips in a small-scale fixed-
429 bed boiler: Validation of the numerical model through in-flame measurements, Fuel. 221 (2018)
430 128–137. doi:https://doi.org/10.1016/j.fuel.2018.02.083.

431 [23] D. Wang, L.-S. Fan, 2 - Particle characterization and behavior relevant to fluidized bed combustion
432 and gasification systems, in: F. Scala (Ed.), Fluid. Bed Technol. Near-Zero Emiss. Combust. Gasif.,
433 Woodhead Publishing, 2013: pp. 42–76. doi:https://doi.org/10.1533/9780857098801.1.42.

434 [24] A. Trubetskaya, G. Beckmann, J. Wadenbäck, J.K. Holm, S.P. Velaga, R. Weber, One way of
435 representing the size and shape of biomass particles in combustion modeling, Fuel. 206 (2017) 675–
436 683. doi:10.1016/j.fuel.2017.06.052.

437 [25] G. Caposciutti, F. Barontini, M. Francesconi, M. Antonelli, Experimental investigation on the fixed
438 bed of a small size biomass boiler, Energy Procedia. 142 (2017) 468–473.
439 doi:10.1016/j.egypro.2017.12.073.

440 [26] D. Neves, H. Thunman, A. Matos, L. Tarelho, A. Gómez-Barea, Characterization and prediction of
441 biomass pyrolysis products, Prog. Energy Combust. Sci. 37 (2011) 611–630.
442 doi:https://doi.org/10.1016/j.pecs.2011.01.001.

443 [27] Robert M. Bethea and R. Russell Rhinehart, Applied Engineering Statistics, 3rd ed., Marcel Dekker,
444 Inc., 1991.

445 [28] J. Riaza, P. Mason, J.M. Jones, J. Gibbins, H. Chalmers, High temperature volatile yield and nitrogen
446 partitioning during pyrolysis of coal and biomass fuels, Fuel. 248 (2019) 215–220.
447 doi:10.1016/J.FUEL.2019.03.075.

448 [29] J. Li, G. Bonvicini, X. Zhang, W. Yang, L. Tognotti, Char Oxidation of Torrefied Biomass at High
449 Temperatures and High Heating Rates, Energy Procedia. 61 (2014) 582–586.
450 doi:10.1016/J.EGYPRO.2014.11.1175.

451 [30] M. Buchmayr, J. Gruber, M. Hargassner, C. Hochenauer, Spatially resolved chemical species
452 concentrations above the fuel bed of a small grate-fired wood-chip boiler, Biomass and Bioenergy.
453 95 (2016) 146–156. doi:http://dx.doi.org/10.1016/j.biombioe.2016.10.004.

454 [31] A. Džiugys, B. Peters, R. Navakas, E. Misiulis, Density segregation on a moving grate, Powder
455 Technol. 305 (2017) 323–332. doi:10.1016/J.POWTEC.2016.09.040.

456

APPENDIX A

Tables A.1 and A.2 report the data presented in Figure 6.

Table A.1: Measured species as a function of λ and ε on different sampling points on the fuel bed surface (Fuel SMD =5.4 mm)

		ε ≈ 2 [-]			ε ≈ 1.5 [-]			
location	λ [-]	0.1	0.5	1	0.1	0.5	1	
LM	CO	0.138	0.138	0.020	0.054	0.255	0.118	[kg/kg$_{vol}$]
	CO_2	0.772	0.777	0.924	0.869	0.655	0.800	
	CH_4	0.042	0.040	0.024	0.034	0.043	0.041	
	H_2	0.035	0.027	0.018	0.025	0.025	0.020	
LS	CO	0.185	0.219	0.187	0.139	0.406	0.301	[kg/kg$_{vol}$]
	CO_2	0.811	0.771	0.799	0.858	0.585	0.686	
	CH_4	<0.001	0.003	0.006	<0.001	0.002	0.005	
	H_2	0.003	0.007	0.007	0.003	0.007	0.007	
CM	CO	0.158	0.201	0.120	0.024	0.220	0.206	[kg/kg$_{vol}$]
	CO_2	0.757	0.764	0.794	0.970	0.677	0.685	
	CH_4	0.046	0.020	0.044	0.005	0.038	0.049	
	H_2	0.025	0.013	0.025	0.001	0.050	0.041	
CS	CO	0.278	0.100	0.293	0.176	0.336	0.347	[kg/kg$_{vol}$]
	CO_2	0.711	0.895	0.685	0.819	0.650	0.645	
	CH_4	0.004	<0.001	0.010	<0.001	0.005	0.002	
	H_2	0.006	0.005	0.011	0.004	0.008	0.006	
RM	CO	0.052	0.012	0.059	<0.001	0.193	0.164	[kg/kg$_{vol}$]
	CO_2	0.938	0.982	0.934	0.999	0.695	0.754	
	CH_4	0.006	0.005	0.004	<0.001	0.052	0.038	
	H_2	0.004	0.002	0.004	<0.001	0.040	0.028	
RS	CO	<0.001	<0.001	0.019	<0.001	0.141	0.077	[kg/kg$_{vol}$]
	CO_2	0.999	0.999	0.980	0.999	0.814	0.896	
	CH_4	<0.001	<0.001	<0.001	<0.001	0.022	0.014	
	H_2	0.001	0.001	0.001	<0.001	0.016	0.008	

Table A.2: Measured species as a function of λ and ε on different sampling points on the fuel bed surface (Fuel SMD = 2.8 mm)

		$\varepsilon \approx 2$ [-]			$\varepsilon \approx 1.5$ [-]			
location	λ [-]	0.1	0.5	1	0.1	0.5	1	
LM	CO	0.153	<0.001	0.058	<0.001	0.137	0.051	[kg/kg$_{vol}$]
	CO_2	0.766	0.964	0.903	0.982	0.766	0.899	
	CH_4	0.033	0.018	0.017	0.011	0.038	0.025	
	H_2	0.032	0.009	0.017	0.002	0.039	0.018	
LS	CO	0.283	0.013	0.255	0.008	0.269	0.298	[kg/kg$_{vol}$]
	CO_2	0.702	0.983	0.741	0.992	0.721	0.684	
	CH_4	0.007	0.002	0.001	<0.001	0.003	0.008	
	H_2	0.007	0.002	0.004	<0.001	0.006	0.007	
CM	CO	0.215	0.076	0.142	<0.001	0.248	0.246	[kg/kg$_{vol}$]
	CO_2	0.766	0.884	0.794	0.978	0.646	0.662	
	CH_4	0.010	0.025	0.038	0.018	0.051	0.046	
	H_2	0.008	0.010	0.019	0.002	0.036	0.038	
CS	CO	0.192	0.104	0.101	0.066	0.317	0.216	[kg/kg$_{vol}$]
	CO_2	0.805	0.887	0.895	0.929	0.661	0.732	
	CH_4	<0.001	0.005	<0.001	0.003	0.009	0.019	
	H_2	0.004	0.005	0.004	0.002	0.012	0.027	
RM	CO	0.023	0.015	0.009	<0.001	0.099	0.055	[kg/kg$_{vol}$]
	CO_2	0.968	0.979	0.985	0.999	0.889	0.928	
	CH_4	0.005	0.004	0.005	<0.001	0.003	0.006	
	H_2	0.004	0.002	0.002	<0.001	0.009	0.010	
RS	CO	<0.001	<0.001	0.001	<0.001	<0.001	0.025	[kg/kg$_{vol}$]
	CO_2	0.999	0.999	0.997	0.999	0.999	0.970	
	CH_4	0.001	<0.001	<0.001	<0.001	<0.001	0.003	
	H_2	<0.001	0.001	0.001	<0.001	<0.001	0.003	

Table A.3 shows the data presented in Figure 7. The average values (ave) and their standard deviation (std), calculated over the different operating conditions, are reported for each sample location.

Table A.3: Volatile gas species composition in different locations for the SMD employed

location		SMD = 8.0 mm						SMD = 5.9 mm						SMD = 2.8 mm					
		CO	CO_2	CH_4	H_2	C_2H_4	C_2H_6	CO	CO_2	CH_4	H_2	C_2H_4	C_2H_6	CO	CO_2	CH_4	H_2	C_2H_4	C_2H_6
		[kg/kg_{vol}]						[kg/kg_{vol}]						[kg/kg_{vol}]					
LM	ave	0.200	0.700	0.050	0.029	0.020	0.004	0.120	0.800	0.037	0.025	0.016	0.002	0.070	0.880	0.024	0.020	0.009	0.002
	std	0.080	0.080	0.009	0.007	0.008	0.002	0.080	0.090	0.008	0.006	0.003	0.001	0.070	0.090	0.011	0.010	0.006	0.001
LS	ave	0.210	0.790	<0.001	0.004	<0.001	<0.001	0.240	0.750	0.003	0.006	<0.001	<0.001	0.190	0.800	0.004	0.005	<0.001	<0.001
	std	0.150	0.160	0.001	0.003	0.001	<0.001	0.100	0.100	0.003	0.002	<0.001	<0.001	0.140	0.140	0.003	0.003	<0.001	<0.001
CM	ave	0.190	0.710	0.050	0.027	0.013	0.005	0.150	0.770	0.034	0.026	0.009	0.003	0.150	0.790	0.031	0.020	0.005	0.002
	std	0.080	0.070	0.006	0.004	0.006	0.001	0.070	0.110	0.017	0.018	0.006	0.002	0.100	0.130	0.016	0.020	0.005	0.002
CS	ave	0.350	0.630	0.007	0.010	<0.001	<0.001	0.260	0.730	0.004	0.007	<0.001	<0.001	0.170	0.800	0.006	0.009	0.001	0.001
	std	0.060	0.060	0.009	0.005	<0.001	<0.001	0.100	0.100	0.004	0.002	<0.001	<0.001	0.090	0.100	0.007	0.010	0.002	0.001
RM	ave	0.140	0.820	0.017	0.015	0.002	0.002	0.080	0.880	0.020	0.010	0.005	0.002	0.030	0.960	0.004	0.004	<0.001	<0.001
	std	0.070	0.090	0.009	0.008	0.001	0.001	0.080	0.130	0.020	0.020	0.007	0.002	0.040	0.040	0.002	0.004	<0.001	<0.001
RS	ave	0.080	0.900	0.011	0.009	0.001	0.001	0.040	0.950	0.010	0.004	0.001	0.001	<0.001	0.990	0.001	0.001	<0.001	<0.001
	std	0.070	0.090	0.011	0.009	0.002	0.001	0.060	0.080	0.010	0.006	0.002	0.001	0.010	0.010	0.001	0.001	<0.001	<0.001

469